

See discussions, stats, and author profiles for this publication at: <https://www.researchgate.net/publication/40678738>

# Formation of ([HIPTN<sub>3</sub>N]Mo(III)H) by heterolytic cleavage of H<sub>2</sub> as established by EPR and ENDOR spectroscopy

ARTICLE *in* INORGANIC CHEMISTRY · DECEMBER 2009

Impact Factor: 4.76 · DOI: 10.1021/ic902006v · Source: PubMed

CITATIONS

17

READS

30

## 5 AUTHORS, INCLUDING:



**Robert Adam Kinney**

U.S. Department of Energy

11 PUBLICATIONS 260 CITATIONS

SEE PROFILE



**Dennis G. H. Hetterscheid**

Leiden University

43 PUBLICATIONS 953 CITATIONS

SEE PROFILE



**Richard Schrock**

Massachusetts Institute of Technology

296 PUBLICATIONS 14,447 CITATIONS

SEE PROFILE

Published in final edited form as:

*Inorg Chem.* 2010 January 18; 49(2): 704–713. doi:10.1021/ic902006v.

## Formation of {[HIPTN<sub>3</sub>N]Mo(III)H}<sup>−</sup> by Heterolytic Cleavage of H<sub>2</sub> as Established by EPR and ENDOR Spectroscopy

R. Adam Kinney<sup>†</sup>, Dennis G.H. Hetterscheid<sup>‡</sup>, Brian S. Hanna<sup>‡</sup>, Richard R. Schrock<sup>‡</sup>, and Brian M. Hoffman<sup>†</sup>

<sup>†</sup>Department of Chemistry, Northwestern University, 2145 Sheridan Road, Evanston, Illinois 60208, USA

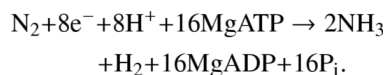
<sup>‡</sup>Department of Chemistry, Massachusetts Institute of Technology, Cambridge, Massachusetts 02139, USA

### Abstract

**MoN<sub>2</sub>** (**Mo** = [(HIPTNCH<sub>2</sub>CH<sub>2</sub>)<sub>3</sub>N]Mo, where HIPT = 3,5-(2,4,6-*i*-Pr<sub>3</sub>C<sub>6</sub>H<sub>2</sub>)<sub>2</sub>C<sub>6</sub>H<sub>3</sub>) is the first stage in the reduction of N<sub>2</sub> to NH<sub>3</sub> by **Mo**. Its reaction with dihydrogen in fluid solution yields '**MoH<sub>2</sub>**', a molybdenum-dihydrogen compound. In this report, we describe a comprehensive EPR and <sup>1/2</sup>H/<sup>14</sup>N ENDOR study of the product of the reaction between **MoN<sub>2</sub>** and H<sub>2</sub> that is trapped in frozen solution, **1**. EPR spectra of **1** show that it has a near-axial g tensor, **g** = [2.086, 1.961, 1.947], with dramatically reduced g-anisotropy relative to **MoN<sub>2</sub>**. Analysis of the g-values reveal that this anion has the Mo(III), [d<sub>xz</sub>, d<sub>yz</sub>]<sup>3</sup> orbital configuration, as proposed for the parent **MoN<sub>2</sub>** complex, and that it undergoes a strong pseudo-Jahn-Teller (PJT) distortion. Simulations of the 2D 35 GHz <sup>1,2</sup>H ENDOR pattern comprised of spectra taken at multiple fields across the EPR envelope (2 K) show that **1** is the [MoH]<sup>−</sup> anion. 35 GHz Mims pulsed <sup>2</sup>H ENDOR spectra of **1** prepared with <sup>2</sup>H<sub>2</sub> shows the corresponding <sup>2</sup>H<sup>−</sup> signal, with a substantial deuterium isotope effect in a<sub>iso</sub>. Radiolytic reduction of a structural analogue, **Mo(IV)H**, at 77 K, confirms the assignment of **1**. Analysis of the 2D <sup>14</sup>N ENDOR pattern for the ligand amine nitrogen further reveals the presence of a linear N<sub>ax</sub>-Mo-H<sup>−</sup> molecular axis that is parallel to the unique magnetic direction (g<sub>1</sub>). The ENDOR pattern of the three equatorial nitrogens is well-reproduced by a model in which the Mo-N<sub>eq</sub> plane has undergone a static, not dynamic, PJT distortion, leading to a range of hyperfine couplings for the three N<sub>eq</sub>. The finding of a nearly axial hyperfine coupling tensor for the terminal hydride bound **Mo** supports the earlier proposal that the two exchangeable hydrogenic species bound to FeMo-cofactor of the nitrogenase turnover intermediate that has accumulated four electrons/protons (E<sub>4</sub>) are hydrides that bridge two metal ions, not terminal hydrides.

### Introduction

In nature, dinitrogen is reduced to ammonia by nitrogenase enzymes, the most studied and best known being the FeMo nitrogenase.<sup>1–7</sup> The reaction proceeds according to the stoichiometry



**Supporting Information Available:** One figure (Figure S1) showing Mims <sup>2</sup>H ENDOR, and a description of the experiment. This material is available free of charge at <http://pubs.acs.org>.

A curious feature of this process is the apparently obligatory formation of a mole of dihydrogen per equivalent of dinitrogen reduced,<sup>8</sup> corresponding to a 75% yield of ammonia in terms of reducing equivalents employed. Under ambient conditions more than one equivalent of H<sub>2</sub> is formed and yields of ammonia vary between 40 and 60%.<sup>9-11</sup> How dihydrogen is formed and the extent to which its formation is coupled to the reduction of dinitrogen is still unknown. What is known with certainty is that dihydrogen inhibits dinitrogen reduction.<sup>9-11</sup>

In 2003 it was shown that dinitrogen could be reduced catalytically to ammonia with protons and electrons by molybdenum complexes that contain the [HIPTN<sub>3</sub>N]<sup>3-</sup> ligand ([HIPTN<sub>3</sub>N]<sup>3-</sup> = [(HIPTNCH<sub>2</sub>CH<sub>2</sub>)<sub>3</sub>N]<sup>3-</sup>, where HIPT is 3,5-(2,4,6-*i*-Pr<sub>3</sub>C<sub>6</sub>H<sub>2</sub>)<sub>2</sub>C<sub>6</sub>H<sub>3</sub>), examples being [HIPTN<sub>3</sub>N]MoN<sub>2</sub>, [HIPTN<sub>3</sub>N]Mo-N=NH, and [HIPTN<sub>3</sub>N]MoNH<sub>3</sub>.<sup>12</sup> In the [HIPTN<sub>3</sub>N]Mo (**Mo**) system, dinitrogen binds end-on to a single Mo and is reduced by repeated alternating additions of a proton and an electron in the manner first proposed by Chatt.<sup>13</sup> Ammonia is formed selectively (no hydrazine is detected) with an efficiency of 55-65% in electrons. The remaining reducing equivalents are used to form dihydrogen. The amount of dinitrogen that can be reduced is limited to ~4 equivalents under the conditions employed, in large part (it is believed) because the [HIPTN<sub>3</sub>N]<sup>3-</sup> ligand is removed from the metal in the presence of protons and reducing agent.

As dihydrogen is formed along with ammonia, both by the **Mo** catalyst and by the nitrogenase enzyme, the dihydrogen chemistry of **Mo**N<sub>2</sub> is of obvious interest. We recently reported<sup>14</sup> that treatment of **Mo**N<sub>2</sub> with H<sub>2</sub> gas generates '**Mo**H<sub>2</sub>', which is possibly an actual H<sub>2</sub> complex or possibly the Mo(V) product of oxidative addition of H<sub>2</sub> to the Mo(III) complex formed by loss of N<sub>2</sub>. We further postulated that rapid H/D scrambling observed in mixtures of H<sub>2</sub>, D<sub>2</sub>, and **Mo**H<sub>2</sub> occurs because '**Mo**H<sub>2</sub>' is in equilibrium with a complex formed by heterolytic cleavage of H<sub>2</sub>, presumed to be a hydrido-Mo(III) with the proton bound to one of the amides. This complex in turn was thought to be in equilibrium with an 'arm-off' complex that may be unstable to loss of the tris-amidoamine ligand.

As a complement to these solution studies we have carried out a comprehensive EPR and <sup>1/2</sup>H/<sup>14</sup>N ENDOR study of the product of the reaction between **Mo**N<sub>2</sub> and H<sub>2</sub> that is trapped in frozen solution, **1**. This species is particularly relevant as a biomimetic complex in that it is paramagnetic and binds an H<sub>2</sub>-derived species. Its characterization thus provides constraints in the analysis of the four-electron reduced (E<sub>4</sub>) state of the molybdenum-iron (MoFe) protein of nitrogenase,<sup>15</sup> whose active-site molybdenum-iron cofactor (FeMo-co) has been shown to contain two chemically identical, symmetry related hydrogenic species with large isotropic hyperfine couplings.<sup>16</sup> The ENDOR measurements of **1** reveal that it is the anionic, hydrido-Mo(III) product of heterolytic cleavage of H<sub>2</sub> (Scheme 1); we discuss its EPR spectrum in terms of the Jahn-Teller Effect (JTE) expected for a low-spin Mo(III) in a trigonal environment.

## Materials and Methods

### Sample Preparation

The **Mo**N<sub>2</sub> complex in solution was converted to **Mo**(III)H<sub>2</sub> by treatment with H<sub>2</sub> gas, as described;<sup>14</sup> solutions of **Mo**(III)H<sub>2</sub> were also prepared by treating solid **Mo**N<sub>2</sub> with H<sub>2</sub> gas, as described,<sup>14</sup> then dissolving in the desired solvent. Upon freezing, the two types of solution gave identical EPR spectra. Solutions of **Mo**(IV)H were prepared as described<sup>17</sup> then frozen in liquid nitrogen for cryoreduction and subsequent EPR/ENDOR measurements. The **Mo**(IV) H solutions were cryoreduced at 77 K to form [**Mo**(III)H]<sup>-</sup> by γ-irradiation.<sup>18</sup>

## EPR and ENDOR Spectroscopy

X-band EPR was obtained on a modified Bruker ER200 series CW spectrometer with an Oxford Instruments ESR 910 continuous He flow cryostat. Spin quantitations involved double integrations and comparison to a CuSO<sub>4</sub> standard (10.2 mM CuSO<sub>4</sub>, 0.1 M NaCl, and 10 mM EDTA in 80:20 (v/v) water:glycerol) by standard methods.<sup>19</sup> The concentration of **1** was determined by measuring the total concentration of S = ½ centers at 4 K, then subtracting the concentration of impurity S = ½ centers as measured at 77 K, a temperature at which the EPR response from **1** is negligible.

35 GHz pulsed and CW EPR and ENDOR spectra were obtained at ~2K on locally-constructed instruments described in detail previously.<sup>20-22</sup> The CW measurements employed 100 kHz field modulation and dispersion mode detection under rapid passage conditions. ENDOR spectra employed broadening of the RF to 100 kHz to improve signal-to-noise.<sup>23</sup> Pulsed ENDOR spectra were collected with both Mims and Davies microwave pulse sequences:  $\pi/2 - \tau - \pi/2 - T - \pi/2 - \tau - echo$  and  $\pi - T - \pi/2 - \tau - \pi - \tau - echo$ , respectively, where T is the time interval during which the RF pulse is applied.<sup>24</sup> Data acquisition for all pulse experiments utilized the SpecMan software package<sup>25</sup> (<http://specman.4epr.com>) in conjunction with a SpinCore PulseBlaster ESR\_PRO 400 MHz word generator and an Agilent Technologies Acquiris DP235 500 MS/sec digitizer.

For a single molecular orientation and for nuclei with nuclear spin of  $I = 1/2$  (<sup>1</sup>H), the ENDOR transitions for the  $m_s = \pm 1/2$  electron manifolds are observed at frequencies dictated by the equation,

$$\nu_{\pm} = |\nu_n \pm A/2|$$

where  $\nu_n$  is the nuclear Larmor frequency, and A is the orientation-dependent hyperfine coupling. For  $I \geq 1$  (<sup>2</sup>H, <sup>14</sup>N), the two ENDOR lines are further split by the orientation-dependent nuclear quadrupole interaction (3P). The peaks are then observed at frequencies dictated by a modified version of the equation above,

$$\nu_{\pm,\pm} = |\nu_{\pm} \pm 3P/2|$$

In the Mims experiment, the ENDOR intensities are modulated by the response factor inherent to the experiment, which is a function of the product  $A\tau$ , and given by the equation,

$$R[1 - \cos(2\pi A\tau)]$$

When  $A\tau = n$  ( $n = 0, 1, 2, \dots$ ), the ENDOR response is at a minimum, resulting in hyperfine ‘suppression holes’ in the Mims spectra.

At the low and high field edges of the EPR spectrum ( $g_1$  and  $g_3$ , respectively), ENDOR interrogates only a single molecular orientation (‘single-crystal-like’ position). At intermediate fields, however, ENDOR interrogates a well-defined subset of molecular orientations. By analyzing a 2D field-frequency (‘orientation-selective’) pattern of ENDOR spectra taken at numerous fields across the EPR envelope, it is generally possible to elucidate the complete hyperfine and quadrupole tensor principal values and their orientations relative to **g**.<sup>26, 27</sup>

## Hyperfine Sign determination

Signs of the hyperfine couplings measured from ENDOR spectra (more specifically, the sign of  $g_{\text{Nuc}}A_{\text{Nuc}}$ ) were obtained by the Pulse-Endor-SaTuration-REcovery (PESTRE) protocol,<sup>28</sup> a pulse sequence comprised of multiple Davies ENDOR sequences, carried out in three distinct experimental phases: (I) an EPR saturation phase (RF off) of 100 Davies sequences whose spin-echo intensities quickly converge to the steady-state 'baseline' (BSL); (II) an ENDOR perturbation phase of 24 sequences, in which each sequence contains a fixed RF set at one or the other of the branches of the ENDOR spectrum; (III) and an EPR recovery phase (RF off) of 388 sequences during which the spin echo corresponds to the spin-echo 'dynamic reference level' (*drl*) associated with ENDOR-induced spin polarization created in the second phase, with the *drl* relaxing to the BSL during this phase. In the slow-relaxation regime, the sign of  $A_{\text{Nuc}}$  is unambiguously given by the sign of the difference between the *drl* and BSL echo intensities as observed for *either* ENDOR branch. The exact time-dependent solution<sup>28</sup> of the master equation<sup>29, 30</sup> for the electron/nuclear spin populations after each Davies pulse sequence in a multi-pulse sequence shows that when  $A_{\text{Nuc}} > 0$  (and  $g_{\text{Nuc}} > 0$ ): if  $\nu_+$  is being interrogated, the *drl* relaxes to the BSL from *below*; when  $\nu_-$  is being interrogated, the *drl* relaxes to the BSL from *above*. When  $A_{\text{Nuc}} < 0$ , the opposite behavior is observed.

## Results

### EPR Measurements of **1**

Figure 1 shows a reference X-band EPR spectrum of **MoN**<sub>2</sub> in frozen toluene solution at 4 K. It has an axial, strongly anisotropic g-tensor,  $g_2 = 3.03 > g_e > g_x = 1.61$ , that is associated with the Jahn-Teller (JT) distortion of the low-spin ( $S = 1/2$ ) orbitally-degenerate Mo(III) ion in an  $[e^3]$  orbital configuration.<sup>31</sup> Upon freezing a solution of **MoH**<sub>2</sub> in toluene or 1:9 2-Me THF:THF solution, prepared by either method described above, the **MoN**<sub>2</sub> signal is found to have disappeared, and been replaced by that of the trapped product (**1**) of reaction between **MoN**<sub>2</sub> and H<sub>2</sub> (Figure 1). This spectrum again is almost axial, with  $g_1 > g_e > g_2 \sim g_3$ , but with the components of **g** far closer to the free-electron g-value: **g** = [2.086(18), 1.961(11), 1.947(8)].

Quantitation of the EPR signal of **1** relative to a CuSO<sub>4</sub> standard shows that the conversion from **MoN**<sub>2</sub> to **1** is far from quantitative, typically under half, with most of the parent **MoN**<sub>2</sub> complex being converted to an unidentified, EPR-silent material; in addition, a relatively weak, unassigned  $S = 1/2$  signal can be seen superimposed on the majority signal (Figure 1, Inset). Frozen-solution spectra of **1** in different solvents differ minimally, unlike the case for **MoN**<sub>2</sub>. As a frozen solution of **1** is warmed above 4 K, its signal broadens and weakens, disappearing by 70 K and leaving the weak impurity signal. During this process,  $g_1$  of **1** decreases slightly, from 2.090 to 2.085. For reasons to be discussed below, solutions of **1** in 1:9 2-Me THF:THF were saturated with the salts [Bu<sub>4</sub>N][BAR<sub>F</sub>] or Na[BAR<sub>F</sub>]. This caused only small changes to the principal g-values, ~ 0.001-0.003.

The g-values of **1** are consistent with its assignment as a Mo(III) metal center, in that the unique g-value ( $g_1$ ) is greater than the free-electron g-value, rather than less, as would be expected for a Mo(V) center. With a near-axial g-tensor, the unique g value ( $g_1$ ) is expected to lie roughly parallel to the idealized three-fold molecular symmetry, thus coinciding with the Mo-N<sub>ax</sub> bond of the **Mo** system and perpendicular to the plane defined by the Mo-N<sub>amido</sub> bonds of the HIPTN<sub>3</sub>N<sup>3-</sup> ligand.

It is useful to discuss the g-values of **1** in terms of the influence of a linear JT distortion on the Mo(III)  $[e^3]$  configuration, following the treatment presented for **[Mo]N**<sub>2</sub>.<sup>31</sup> This incorporates linear vibronic coupling of the d-electrons into a single composite ('interaction')  $e_2$  mode

(effective force-constant  $K$ , and effective coupling parameter  $F$ ), which competes with the spin-orbit coupling (SOC) and results in a ‘pseudo Jahn-Teller effect’, PJTE. A distortion,  $\rho$ , along the interaction coordinate mixes the  $e_1$  orbitals and lowers the vibronic energy relative to the symmetric structure. Ignoring SOC to the other  $d$  orbitals, the  $g$ -values are determined by  $r$ , the ratio of the off-diagonal matrix element that generates the splitting of the degenerate  $[e] = [d_{xz}, d_{yz}]$  orbitals,  $V_\delta$ , to the SOC parameter,  $\lambda$ , eq 1;  $V_\delta$  is equal to the sum of the equilibrium JT distortion energy,  $V_{JT}$ , plus a possible ‘environmental energy’,  $V_E$ . For example, in the case of  $\text{MoN}_2$ ,  $V_E$  is associated with solvent interactions, denoted by  $V_L$ . The ratio  $r$  is conveniently used to define a fictitious angle,  $2\theta$ ,

$$r \equiv \tan \quad 2\theta \equiv 2V_\delta/\lambda \equiv 2[V_{JT} + V_E]/\lambda \quad (1)$$

allowing the  $g$ -values to be written in terms of  $2\theta$ :

$$g_{\parallel} = 2(1 + \cos \quad 2\theta) \quad (2a)$$

$$g_{\perp} = (2 \quad \sin \quad 2\theta) \quad (2b)$$

As  $r$  increases,  $2\theta$  increases from 0 (JTE quenched; no distortion) to  $\pi/2$  (strong splitting of  $e_1$  degeneracy; real  $e^1$  orbitals) and the  $g$ -values traverse the range,  $[4 \geq g_{\parallel} \geq 2 \geq g_{\perp} \geq 0]$ . For comparison,  $g_{\parallel} \sim 3$  for  $[\text{Mo}]L$ ,  $L = \text{N}_2/\text{CO}$ , corresponds to  $r \sim 1$ , whereas  $g_{\parallel} = 2.09$  for **1** corresponds to  $r \sim 20$ . Thus, although the  $g$ -shifts are much smaller than for  $\text{MoN}_2$ , the  $g$ -tensor for **1** is compatible with an  $[e^3]$  orbital configuration, but with a much larger splitting of the  $e$ -orbital degeneracy than that experienced by  $\text{MoN}_2$ . Indeed, the extent of the splitting of the  $d_\pi$  orbitals is so great that one could alternatively treat the value for  $g_{\parallel}$  in terms of an electron in a single, real,  $d_\pi$  orbital coupled by SOC to the other  $d_\pi$  orbital, to 2<sup>nd</sup> order.<sup>19</sup> However, the Discussion, below, makes it clear why the PJT perspective is useful. In either case, the slight splitting of  $g_2, g_3$  for **1** is attributable to the influence of 2<sup>nd</sup>-order contributions to  $\mathbf{g}$  from other  $d$  orbitals.

## <sup>1/2</sup>H ENDOR Measurements of **1**

**Strongly-coupled <sup>1</sup>H derived from H<sub>2</sub>**—The 35 GHz stochastic field-modulation detected CW ENDOR<sup>32</sup> spectrum of **1** obtained at  $g_1$  shows a <sup>1</sup>H doublet centered at the <sup>1</sup>H Larmor frequency and split by a hyperfine interaction of  $|A(^1\text{H})| = 13.4$  MHz (Figure 2). These peaks are absent in the corresponding <sup>1</sup>H spectrum of  $\text{Mo}^2\text{H}_2$  (**1(D)**), while Mims 35 GHz <sup>2</sup>H pulsed ENDOR spectra of **1(D)** show a corresponding <sup>2</sup>H signal. Thus, this ENDOR response is associated with a Mo-bound species that arises from dihydrogen. The <sup>2</sup>H ENDOR hyperfine coupling is approximately, but not precisely, related to the <sup>1</sup>H ENDOR hyperfine coupling by the ratio of the hydrogen and deuterium nuclear  $g$  values:  $g_n(^1\text{H})/g_n(^2\text{H}) = 6.51$ . As seen in Figure 2, in which the x-axes have been scaled by the ratio of nuclear  $g$ -factors, the <sup>2</sup>H ENDOR splitting does not precisely match its <sup>1</sup>H counterpart. The difference corresponds to a quite substantial isotope effect on the hyperfine couplings,  $(A(^1\text{H})/g_n(^1\text{H}))/(A(^2\text{H})/g_n(^2\text{H})) = 1.14$ , which is caused by differences in Mo-<sup>1</sup>H/<sup>2</sup>H zero-point motion that cause differences in spin delocalization.<sup>33</sup>

To determine the hyperfine tensor ( $\mathbf{A}$ ) of the Mo-bound hydrogenic species, we collected a full 2D field-frequency pattern comprised of <sup>1</sup>H spectra taken at multiple fields across the EPR spectrum (Figure 3). Simulation of this pattern yields excellent agreement with experiment for a model with a single (type of) <sup>1,2</sup>H whose roughly axial  $\mathbf{A}$  tensor is coaxial with  $\mathbf{g}$ :  $\mathbf{A} = [A_1,$



$A_2, A_3] = [-13.0(1), 35.8(3), 42.5(2)]$  MHz ( $A_1$  parallel to  $g_1$ ), corresponding to an isotropic coupling,  $a_{\text{iso}} = -30.5$  MHz, and an anisotropic (dipolar) interaction,  $\mathbf{T} = +[17.5, -5.5, -12]$  MHz. The relative signs of the components of the  $\mathbf{A}$  and  $\mathbf{T}$  tensors are determined by the simulations.<sup>34</sup>

The absolute signs initially were assigned under the assumption that  $\mathbf{T}$  is dominated by the through-space electron-nuclear dipolar interaction with the Mo(III) electron spin, in which case  $T_1 > 0$ . This assignment has been confirmed by application of the PESTRE technique, in which the sign of a hyperfine interaction is determined by monitoring the response of the electron-nuclear spin system to multiple Davies sequences at fixed RF frequency. Figure 5 shows the traces obtained for PESTRE ‘three-phase’ multi-sequences that separately include RF applied to the  $\nu_+$  and  $\nu_-$  ENDOR peaks of the strongly-coupled  $^1\text{H}$  at  $g_2$ . In phase I (no RF), both traces have reached the steady-state electron spin-echo baseline (BSL); in phase II, the RF is applied to a particular branch of the spectrum and converts the spin populations and spin-echo response to their steady-state ENDOR values; in phase III (no RF), the electron-nuclear spin populations give rise to a spin-echo signal denoted as the dynamic reference level (*drl*), which relaxes to the BSL. In these Phase III traces, the  $\nu_+$  *drl* relaxes to the BSL from *above*, while the  $\nu_-$  *drl* relaxes from *below*. *Either* observation is an unambiguous indication that  $A(g_2) < 0$ . This verifies the above assignment for the principal values of  $\mathbf{A}$  and  $\mathbf{T}$ , and that  $a_{\text{iso}} < 0$ .<sup>28</sup>

The presence of a large isotropic coupling requires that the exchangeable hydrogenic species is bound to Mo, while  $a_{\text{iso}} < 0$  indicates that spin is delocalized by spin polarization of the 2-electron M-H bond, and not by direct overlap between a partially filled metal-ion orbital and the 1s orbital of H. The assignment of  $g_1$  as lying along the symmetry axis of the parent  $\text{MoN}_2$ , in conjunction with an ENDOR analysis showing coaxial  $\mathbf{A}$  and  $\mathbf{g}$  tensors for a single type of hydrogenic species, with  $T_{\text{max}} = T_1$ , suggests a model in which heterolytic cleavage of  $\text{H}_2$  has yielded a single hydride bound to Mo(III), with a linear  $\text{N}_{\text{ax}}\text{-Mo-H}^-$  linkage (Figure 3),  $\sigma$  bonding between the hydrido 1s and Mo  $d_z^2$  orbital, and polarization of this bond by the  $\pi$  electron spin in  $d_{xz}, d_{yz}$  of Mo. The point-dipole approximation for the anisotropic  $^1\text{H}$  hyperfine coupling is not highly accurate,<sup>35</sup> but for reference purposes, it would yield a Mo-H bond length of  $\lesssim 2$  Å.

To test this model we compared the experimental 2D ENDOR pattern to those expected for either a dihydrogen complex or a Mo(V)-dihydride complex (Figure 4 and Figures S3-S4). These alternate models each would have two magnetically equivalent H atoms, so ENDOR measurements would detect only a single type of hydrogenic species, consistent with experiment. However, the three models would yield different 2D ENDOR patterns, because each has a distinct value for the angle ( $\beta$ ) that the Mo-H vector(s) make with the  $g_1$  (symmetry) axis: for on-axis  $\text{MoH}^-$ ,  $\beta = 0^\circ$ ; for a dihydrogen complex, reference X-ray structures indicate an expected value of  $\beta = 10^\circ$  for each of the equivalent H atoms;<sup>36</sup> for a dihydride,  $\beta = 30\text{--}45^\circ$ .<sup>37, 38</sup>

Simulations were generated in which the value of  $\beta$  was increased from  $0^\circ$  to  $30^\circ$ . At all fields away from the high and low-field edges of the EPR spectrum, as  $\beta$  increases from zero, these spectra show a progressive increase in the breadth of the simulated ENDOR responses and the appearance of new resolved features. Figure 4 presents spectra calculated for a representative field that is sensitive to  $\beta$  ( $g = 1.99$ ), using the values of  $\beta$  associated with the three structural models,  $\beta = 0^\circ, 10^\circ$ , and  $30^\circ$ . Whereas  $\beta = 0^\circ$  gives an essentially perfect reproduction of the entire 2D pattern, it is clear that even with  $\beta = 10^\circ$ , the simulations predict that the ENDOR pattern would split into two well-resolved peaks, with the maximum splitting observed at  $g = 2.017$ ; increasing the linewidth to merge the peaks would then give an overall feature far broader than observed. Naturally, the problem is exacerbated for  $\beta = 30^\circ$ . Overall, the

simulations show that the experimental observations rule out any model for which  $\beta \geq 5^\circ$ , thus affirming the assignment of **1** as a Mo(III)-H<sup>-</sup> center.

**Search for  $^2\text{H}^+$** —Heterolytic cleavage of H<sub>2</sub> to generate hydrido-Mo(III) also generates a proton. If this remains bound to **Mo**, it would likely bind to one of the amido nitrogens of the HIPTN<sub>3</sub>N<sup>3-</sup> ligand. Simple considerations of geometry indicate that the amido N-H would be  $\sim 2.5$  Å from the molybdenum and would exhibit a maximum dipolar coupling,  $T_{\text{max}}(^2\text{H}) \sim 1.6$  MHz, and thus should be readily observable. An extensive search was conducted for the signals from such a species using the Mims  $^2\text{H}$  ENDOR protocol with a wide range of spectroscopic conditions. Under *no* conditions at *any* field within the EPR envelope did the  $^2\text{H}$  Mims pulsed ENDOR of **MoD**<sub>2</sub> show *any* response that could be reasonably assigned to such a deuteron, as illustrated by the spectrum collected at  $g_1$  (Figure 2) and in the supplementary material (Figure S4). The absence of an ENDOR response from a weakly coupled deuteron suggests that the proton is transferred to a basic, EPR-silent species during the generation, cooling, and freezing of **MoH**<sub>2</sub>, and that the species **1** trapped in frozen solution in fact is the [Mo(III)H]<sup>-</sup> anion.

### EPR and ENDOR Studies of Cryoreduced MoH (2)

To verify this assignment of **1**, a frozen solution of **Mo(IV)H** (**2**) ( $d^2$ ; EPR-silent) was radiolytically reduced at 77 K with the goal of directly generating the [Mo(III)H]<sup>-</sup> anion. Although no crystal structure of **2** is available, its precursor, **MoCl**, has been crystallographically characterized.<sup>39</sup> In this structure, the N<sub>ax</sub>-Mo-Cl axis is normal to the plane of the equatorial nitrogens. As complex **2** is synthesized from **MoCl** via ligand substitution of the axial chloride with a hydride from the donor species LiBHET<sub>3</sub>,<sup>17</sup> the two should share the same structure, with the Cl<sup>-</sup> replaced by the H<sup>-</sup>.

Figure 6 shows overlaid EPR spectra of **1** and of **2**, both before and after cryoreduction. Untreated **2** shows a weak EPR signal that is nearly identical to that of **1**. Upon cryoreduction, this signal increases approximately five-fold, indicating that this signal is associated with the [MoH]<sup>-</sup> anion; its  $g$ -values of [2.086, 1.961, 1.949] are the same as those of **1**. A comparison of the  $^1\text{H}$  2D ENDOR patterns of cryoreduced **2** and of **1**, as illustrated by the  $^1\text{H}$  ENDOR spectra at  $g_2$  (Figure 6, inset), shows that the two species give identical spectra at all fields. These EPR and ENDOR experiments thus establish that **1** indeed is the [Mo(III)H]<sup>-</sup> anion.

### $^{14}\text{N}$ ENDOR Measurements of **1**

Figure 7 presents  $^{14}\text{N}$  Davies pulsed ENDOR spectra of **1** collected at the low-field ( $g_1 = 2.086$ ) and high-field ( $g_3 = 1.947$ ) edges of its EPR envelope. These two spectra reveal features from two distinct types of nitrogen signals: sharp, well-defined signals that are assigned to the axial amino nitrogen (N<sub>ax</sub>); broader signals that are attributed to the combined ENDOR response of the three ‘equatorial’ amido nitrogens (N<sub>eq</sub>) of the HIPTN<sub>3</sub>N<sup>3-</sup> ligand. The patterns for the two types of  $^{14}\text{N}$  overlap across the entire EPR envelope, but because the features from the axial nitrogen are significantly sharper, the two signals are easily distinguished at all fields. In addition, the spectra clearly show  $\Delta m_I = \pm 2$  “double quantum” transitions<sup>24</sup> for both the  $\nu_+$  and  $\nu_-$  manifolds of  $^{14}\text{N}_{\text{ax}}$  across the entire EPR envelope (Figure S6), giving an experimentally independent check of our assignments. We note that the  $^{14}\text{N}$  spectra of the [MoH]<sup>-</sup> anions of cryoreduced **2** and of **1** are identical (Figure S5), as required.

**Axial Nitrogen (N<sub>ax</sub>)**—In Figure 7, the  $^{14}\text{N}_{\text{ax}}$  nucleus contributes a sharp, quadrupole-split,  $\nu_+$  doublet at both  $g_3$  and  $g_1$ , with  $A(g_3) = 4$  MHz,  $|3P(g_3)| = 2.7$  MHz (bottom), and  $A(g_1) = 4$  MHz,  $|3P(g_1)| = 5.5$  MHz (top). For the 2D field-frequency pattern of N<sub>ax</sub> (Figure 8 and Figure S6), the ENDOR spectra taken across the EPR envelope are reproduced by simulations that employ an essentially isotropic hyperfine tensor ( $a_{\text{iso}} = 4$  MHz), and an axial quadrupole



tensor ( $\mathbf{P} = [P_1, P_2, P_3] = [-1.82, 0.91, 0.91]$  MHz). The relative signs of the  $P_i$  ( $i = 1-3$ ) are fixed by the simulations; the absolute signs are established as discussed by Lucken.<sup>40</sup>  $\mathbf{P}$  is coaxial with  $\mathbf{g}$ , with the unique value,  $P_1$ , lying along  $g_1$ . The form of  $\mathbf{P}$  is precisely as expected for the coordinated tri-alkyl amino  $N_{ax}$  nitrogen,<sup>40</sup> for which the unique quadrupole direction ( $P_1$ ) must lie along the Mo- $N_{ax}$  bond ( $g_1$ ), as observed. These measurements thus directly confirm the structural model of a linear  $N_{ax}$ -Mo-H<sup>-</sup> axis (Figure 3, inset), with the unique axes of  $\mathbf{g}$ ,  $\mathbf{P}$  for  $N_{ax}$ , and  $\mathbf{A}$  for the hydride all lying along this molecular axis.

**Equatorial Nitrogens ( $N_{eq}$ )**—In the  $^{14}\text{N}$  ENDOR spectrum at  $g_1$  (Figure 7, top), the three  $^{14}\text{N}_{eq}$  nuclei combine to give a single quadrupole-split  $\nu_+$  doublet. Unlike the extremely sharp  $N_{ax}$  signal (FWHM = 0.5 MHz), the individual  $\nu_{+, \pm}$  features for  $^{14}\text{N}_{eq}$  at  $g_1$  are far broader (FWHM = 1.1 MHz). If the anion had precise  $C_3$  symmetry with  $g_1$  as the symmetry axis, the three equatorial nitrogen ligands would be magnetically equivalent when viewed with the field along  $g_1$ , and the  $\nu_+$  doublet would likely be sharp, as it is for  $N_{ax}$ . That this is not the case suggests that the anion is statically distorted from trigonal symmetry, that the hyperfine and/or quadrupole couplings differ for the three  $^{14}\text{N}$ , and that the  $^{14}\text{N}_{eq}$  ENDOR spectrum at  $g_1$  reflects a range of values for one or both of these parameters. If we consider the two extremes, well-defined hyperfine coupling at  $g_1$  but distributed quadrupole couplings, or vice versa, in the first case the breadth of the  $\nu_{+, \pm}$  features would correspond to a hyperfine coupling of  $A(g_1) = 6.6$  MHz and a quadrupole splitting range of  $2.7 \leq |3P(g_1)| \leq 4.5$  MHz, while in the second the breadth would imply a hyperfine range of  $5.4 \leq A(g_1) \leq 7.1$  MHz, with a quadrupole splitting of  $|3P(g_1)| = 3.9$  MHz.

In the spectrum collected at  $g_3$  (Figure 7, bottom), the three  $^{14}\text{N}_{eq}$  combine to give an ENDOR pattern with features that are narrower than at  $g_1$ , with  $A(g_3) \sim 8.8$  MHz and  $|3P(g_3)| \sim 3.8$  MHz, but again, the  $N_{eq}$  features are broader than those of the corresponding  $N_{ax}$  doublet. However, in this case the magnetic field lies in the equatorial plane, and of necessity the angle between the field and the Mo- $N_{eq}$  bond is not the same for all three  $N_{eq}$ . As such, in spectra collected at  $g_3$  the three nuclei could not have the same hyperfine and quadrupole couplings, even if they were physically and chemically equivalent.

To determine the origin of the breadth of the  $^{14}\text{N}_{eq} \nu_{+, \pm}$  feature at  $g_1$  we used the hyperfine suppression effect inherent to the Mims ENDOR technique. For a Mims sequence with pulse interval,  $\tau$ , the  $\nu_+$  ENDOR doublet would be suppressed for nuclei with  $A_1(^{14}\text{N}_{eq}) = n/\tau$  ( $n = 0, 1, 2, \dots$ ) regardless of the value of  $3P_1$ . If suppression is observed for a range of  $\tau$  values, this would imply a corresponding spread in  $A_1(^{14}\text{N}_{eq})$ , while the breadth of a suppression hole would be determined by the spread in values of the quadrupole splitting,  $3P_1$ .

Figure 9 shows a 2D  $\tau$ -frequency plot of Mims ENDOR spectra collected at  $g_1$  over the range  $550 \leq \tau \leq 870$  ns. Both branches of the  $\nu_{+, \pm}$  doublet show sharp suppression holes over the range of pulse intervals,  $\tau$ . The sharp suppression holes indicates that the quadrupole splitting,  $3P_1$ , is well-defined, while suppression over a range in  $\tau$  indicates that the  $^{14}\text{N}_{eq}$  exhibit a corresponding range in  $A(g_1)$ . Thus, the second limiting case noted above applies:  $5.4 \leq A(g_1) \leq 7.1$  MHz, with  $|3P(g_1)| = 3.9$  MHz. A reasonable simulation of the  $^{14}\text{N}_{eq} g_1$  ENDOR spectrum based on such a hyperfine distribution is obtained by modeling it with the summation of ENDOR simulations generated with three equally probable  $A_1$  hyperfine couplings,  $A_1 = \{5.39, 6.25, 7.11\}$  MHz, each with  $|P_1| = 1.33$  MHz (Figure 8, top).

The next step in characterizing the Mo- $N_{eq}$  bonding was determination of the full  $^{14}\text{N}_{eq}$  hyperfine and quadrupole tensors for the three  $^{14}\text{N}_{eq}$  from a 2D field/frequency pattern of  $^{14}\text{N}$  spectra collected across the EPR envelope (Figure 8). For simplicity in analysis, we took the Mo- $N_{eq}$  bonds to be orthogonal to  $g_1$  and trigonally arranged ( $N_{eq}$ -Mo- $N_{eq} = 120^\circ$  for adjacent  $N_{eq}$ ), each with coaxial  $\mathbf{A}$  and  $\mathbf{P}$  tensors whose ( $A_1, P_1$ ) principal axes lie parallel to

$g_1$ , and with the ( $A_3$ ,  $P_3$ ) principal axis for the three N making angles,  $\alpha$ ,  $\alpha + 2\pi/3$ ,  $\alpha + 4\pi/3$ , with  $g_3$ . If we imagine ( $A_3$ ,  $P_3$ ) to lie along the Mo- $N_{eq}$  bond, then  $\alpha$  would represent the rotation of the  $N_{eq}$  equilateral triangle, relative to the  $g_3$  principal axis, with  $\alpha = 0$  placing the Mo- $N_{eq}$  bond of one nitrogen along  $g_3$  (Figure 8, inset). We note, however, that the model does not require that  $A_3$  and  $P_3$  be coincident with Mo- $N_{eq}$ , only that they have the same orientation relative to Mo- $N_{eq}$  for all three equatorial nitrogens. The angle  $\alpha$  turns out to be particularly important in reproducing the ENDOR spectra at fields in the vicinity of  $g_2$  and  $g_3$ . The simplest model that effectively reproduces the pattern assigns to each of the  $N_{eq}$  an equal probability that it has each of the three values of  $A_1 = \{5.39, 6.25, 7.11\}$  MHz determined in the above analysis of the  $g_1$  spectrum, as well as  $|P_1| = 1.33$  MHz. All the other tensor components were assumed to be the same for the three  $N_{eq}$ . This model was implemented by summing the corresponding nine simulations at each  $g$  value.

The outcome of numerous simulation attempts was that the 2D pattern can be well simulated (Figure 8) by combining the nine sets of simulations for interaction tensors with components  $\mathbf{A} = [\{5.39, 6.25, 7.11\}, 5.8, 8.7]$  MHz,  $\mathbf{P} = [-1.33, 0.03, 1.3]$  MHz, and with the  $N_{eq}$  triangle rotated relative to  $g_3$  by the angle  $\alpha = 15^\circ$ . Considering the limited resolution in the ENDOR spectra, and the need to sum multiple spectra from inequivalent  $^{14}\text{N}$ , the use of more complex structural models, for example placing Mo out of the  $N_{eq}$  plane, or allowing for angular distortions within the  $N_{eq}$  plane, is unwarranted. Nonetheless, this range in coupling parameters for the  $N_{eq}$  nuclei is direct evidence for a static JT distortion of the **Mo** equatorial plane.

## Discussion

We have carried out a comprehensive EPR and ENDOR study of the product of reaction between  $[\text{HIPTN}_3\text{N}]\text{MoN}_2$  and  $\text{H}_2$ . Analysis of  $^1\text{H}$  ENDOR spectra taken at multiple fields across the EPR envelope (2 K) shows that the principal species in frozen solution is the  $[\text{MoH}]^-$  anion, **1** (Scheme 1). This anion is assigned as having a Mo(III),  $[d_{xz}, d_{yz}]^3$  orbital configuration, as proposed for the parent **MoN**<sub>2</sub> complex, and therefore is susceptible to a Jahn-Teller (JT) distortion. We first discuss the properties and structure of the  $[\text{MoH}]^-$  anion as determined by  $^{1,2}\text{H}$  and  $^{14}\text{N}$  ENDOR. We next discuss JT effects in the anion in light of the structural results and the  $g$ -tensor of this anion. Lastly, we compare this study of **1** trapped in frozen solution with the recent study of the reaction of  $[\text{HIPTN}_3\text{N}]\text{MoN}_2$  and  $\text{H}_2$  in fluid solution.

### $[\text{MoH}]^-$ (**1**) in frozen solution

$^{1,2}\text{H}$  ENDOR measurements of **1** reveal the presence of a single hydride bound to Mo, the result of heterolytic cleavage of  $\text{H}_2$ . In combination with  $^{14}\text{N}$  ENDOR measurements of the axial amino nitrogen of the  $[\text{HIPTN}_3\text{N}]\text{Mo}$  center, these observations reveal the presence of a structural axis that passes through the hydride, the Mo, and the axial amino nitrogen of the  $[\text{HIPTN}_3\text{N}]^{3-}$  ligand, and that this axis is coincident with the unique magnetic axis ( $g_1$ ) of the molecule. These conclusions are confirmed by EPR and ENDOR measurements ( $^1\text{H}$  and  $^{14}\text{N}$ ) which show that **1** trapped in frozen solution is essentially identical to the anion formed when **Mo(IV)H** (**2**) is radiolytically reduced to the  $[\text{Mo(III)H}]^-$  anion at 77 K.

$^{14}\text{N}$  ENDOR measurements also characterized the three nitrogens of  $[\text{HIPTN}_3\text{N}]^{3-}$  that form an equatorial plane perpendicular, or nearly so, to the  $[\text{H}^--\text{Mo}-\text{N}_{ax}]$  axis. These revealed that the three nitrogens are magnetically similar, as would be expected for a system possessing a pseudo- $C_3$  axis of symmetry, but that they are not equivalent, as would be the case for a trigonally symmetric molecule or one undergoing a dynamic JT distortion. Thus they indicate that the hydride anion instead exhibits a static JT distortion.

### Where is the proton?

The assignment of **1** as a Mo-hydride anion generated by heterolytic cleavage of H<sub>2</sub> raises the question: where is the partner proton generated in parallel? Our initial expectation was that the proton would bind to one of the three basic amido nitrogens of the [HIPTN<sub>3</sub>N]<sup>3-</sup> ligand. However, extensive efforts failed to disclose either a <sup>1</sup>H or <sup>2</sup>H ENDOR signal from this proton, whereas such a proton is readily detected when [Mo]CO is treated with acid (unpublished). Moreover, preliminary DFT computations<sup>41</sup> confirm that such a protonation would decrease the N<sub>ax</sub>-Mo-H<sup>-</sup> angle from 180°, such that either the Mo-N<sub>ax</sub> or Mo-H<sup>-</sup> bonds, and thus either the <sup>1/2</sup>H or the <sup>14</sup>N<sub>ax</sub> hyperfine (and <sup>14</sup>N<sub>ax</sub> quadrupole) tensors could be coaxial with **g**, but not both, contrary to observation.

If the proton formed by H<sub>2</sub> heterolysis does *not* reside on an equatorial nitrogen of the hydrido complex **1**, what, then, is its fate? In the solution study it was proposed that the heterolytically cleaved species (denoted MoHN<sub>H</sub>), itself in equilibrium with 'MoH<sub>2</sub>', further is in equilibrium with an arm-off form, and that this is unstable to decomposition and ligand loss.<sup>14</sup> We suggest that during the process of freezing a sample of 'MoH<sub>2</sub>', free ligand, produced by decomposition either of the MoHN<sub>H</sub> or the 'arm-off' species, or other EPR-silent products of decomposition, accept the proton from MoHN<sub>H</sub>, thereby generating the hydride anion **1**, and that this process pulls the equilibrium involving 'MoH<sub>2</sub>' completely to **1**.

### The Jahn-Teller Effect and the g and Hyperfine Tensors of **1**

The hydrido-Mo(III) anion revealed by ENDOR spectroscopy would have g-values of g<sub>||</sub> = 4, g<sub>⊥</sub> = 0 in its idealized C<sub>3</sub> geometry. Thus, the discussion of the g tensor must be carried out in a different framework than would be the case if it had been found to be either a lower-symmetry H<sub>2</sub> or a dihydrido complex. The decrease in g<sub>||</sub> to g<sub>1</sub> = 2.086 and the increases in g<sub>⊥</sub> to g<sub>2,3</sub> ~ 2, is most informatively discussed in terms of the reduction in symmetry from C<sub>3</sub> as would occur with a PJT distortion, as described by eq 1 and 2, with r ~ 20. The small rhombicity of the g tensor, attributable to the influence of 2<sup>nd</sup>-order contributions to **g** from other d orbitals, should be more pronounced in **1** than in MoN<sub>2</sub> because the absence of a strong π-backbonding axial ligand in **1** should diminish the energy difference between the d(xz,yz)<sup>3</sup> orbitals and the higher-lying empty d(z<sup>2</sup>) orbital, increasing the 2<sup>nd</sup>-order contributions; furthermore, the narrow EPR lines of **1** improve the ability to observe this splitting. This picture is supported by the observation that, unlike MoN<sub>2</sub>, the EPR spectrum of **1** broadens with increasing temperature, indicating that **1** has lower-lying excited states than MoN<sub>2</sub>.<sup>42</sup> The analysis of the <sup>14</sup>N ENDOR signals from the in-plane <sup>14</sup>N<sub>eq</sub> shows that **1** undergoes a localized, not a dynamic, PJT distortion. Localization can be caused by quadratic terms in the vibronic interaction,<sup>43</sup> or by environmental trapping of the distorted configuration(s).

Thus, the complete set of magnetic properties of **1** can be interpreted in terms of a hydrido-Mo(III) anion undergoing a PJT distortion. However, the large value for the linear JT parameter, r (eq 1), for **1** implied by this analysis, compared to that for MoN<sub>2</sub>, is surprising. The obvious explanation for why r for anionic **1** is so large is that **1** experiences a large environmental energy, V<sub>E</sub>. However, this does not appear to represent a 'solvent effect', because, unlike MoN<sub>2</sub>, there is a negligible effect on the EPR spectrum of **1** with solvent variation. Also, it does not seem plausible that the larger value of r simply reflects a larger value of the linear JT term, V<sub>JT</sub>, in the numerator of r (eq 1). This parameter depends on the linear vibronic coupling parameter (F) and the force-constant (K) for the composite JT-active vibration, through the relationship, V<sub>JT</sub> ∝ F<sup>2</sup>/K. The composite vibration likely is associated with the [HIPTN<sub>3</sub>N]<sup>3-</sup> ligand of **Mo**, which is the same for both systems; to the extent that K is associated with the axial ligand, the force constants for Mo-H and Mo-N are expected to differ very little.<sup>17,44,45</sup>

One possible explanation is that anionic **1** forms a tight ion pair with an unidentified counterion, and that  $V_\delta \sim V_E$ , an electrostatic interaction potential between the ions. However, the absence of any significant changes in the g-values for **1** when other cations (salts) were added to the solution, plus the observation of an identical g tensor for **1** formed by cryoreduction of **Mo** (IV)H (**2**) in frozen solution, where a tight ion pair cannot form, makes this proposal unlikely. Instead, we surmise that the inferred decrease in the energy gap between the partially filled d [xz, yz] and the empty d[xy,  $x^2-y^2$ ] in **1**, as compared to **MoN<sub>2</sub>**, allows mixing of these orbitals, leading to a distortion that in effect amounts to an additional PJTE.<sup>46</sup> DFT computations to test this idea, as well as to give deeper insights into the bonding and hyperfine interactions in this unusual  $S = 1/2$  complex, will be reported in due course.

**Summary**—A comprehensive EPR and  $1/2\text{H}/^{14}\text{N}$  ENDOR study of the product of the reaction between **MoN<sub>2</sub>** and **H<sub>2</sub>** (**1**) that is trapped in frozen solution, including the determination of hyperfine signs through the newly developed PESTRE technique, has shown **1** to be the [**Mo** (III)H]<sup>−</sup> anion that forms as a result of heterolytic cleavage of **H<sub>2</sub>**. The measurements show that **1** contains a linear N<sub>eq</sub>—Mo—H<sup>−</sup> axis along which lies the ‘unique’ axis of the g tensor for the complex. Determination of the hyperfine and quadrupole interaction tensors for the three equatorial nitrogens shows that they have similar properties, but that the complex shows a small, static distortion from an idealized trigonal geometry. This distortion is discussed in terms of the PJTE expected for low-spin Mo(III) in a trigonal environment. The generation of this species is discussed in terms of the equilibria between the ‘**MoH<sub>2</sub>**’, **MoHN<sub>H</sub>**, and a previously postulated ‘arm-off’ species, and supports the conclusion that the ‘**MoH<sub>2</sub>**’ complex is in dynamic equilibrium between these several forms. Beyond this, the finding of a nearly axial hyperfine coupling tensor for a hydride bound to molybdenum supports the proposal that hydrogenic species with rhombic hyperfine tensors bound to the FeMo-cofactor of the nitrogenase E<sub>4</sub> intermediate are hydrides that bridge two metal ions, rather than terminal hydrides.<sup>16</sup>

## Supplementary Material

Refer to Web version on PubMed Central for supplementary material.

## Acknowledgments

RAK and BMH thank Dr. Rebecca McNaughton and Dr. Peter Doan for helpful discussions, and Clark Davoust for his technical support. This work has been supported by the NIH (GM 31978, RRS; HL 13531, BMH) and the NSF (MCB0723330, BMH); DGHH thanks The Netherlands Organization for Scientific Research (NWO-CW) for a postdoctoral fellowship

## References

1. Burgess BK, Lowe DL. Mechanism of Molybdenum Nitrogenase. *Chem. Rev* 1996;96:2983–3011. [PubMed: 11848849]
2. Eady RR. Structure-function relationships of alternative nitrogenases. *Chemical Reviews* (Washington, D. C.) 1996;96(7):3013–3030.
3. Howard JB, Rees DC. Structural Basis of Biological Nitrogen Fixation. *Chem. Rev* 1996;96:2965–2982. [PubMed: 11848848]
4. Dos Santos PC, Igarashi RY, Lee H-I, Hoffman BM, Seefeldt LC, Dean DR. Substrate Interactions with the Nitrogenase Active Site. *Accounts of Chemical Research* 2005;38(3):208–214. [PubMed: 15766240]
5. Hardy, RWF.; Bottomley, F.; Burns, RC. *Treatise on Dinitrogen Fixation*. Wiley-Interscience; New York: 1979.
6. Veegeer, C.; Newton, WE. *Advances in Nitrogen Fixation Research*. Dr. W. Junk/Martinus Nijhoff; Boston: 1984.

7. Coughlan, MP. Molybdenum and Molybdenum-containing Enzymes. Pergamon; New York: 1980.
8. Simpson FB, Burris RH. Nitrogen Pressure of 50 Atmospheres Does Not Prevent Evolution of Hydrogen by Nitrogenase. *Science* (Washington, DC, United States) 1984;224:1095–1097.
9. Werland S, Burgess BK, Stiefel EI, Newton WE. Nitrogenase reactivity: effects of component ratio on electron flow and distribution during nitrogen fixation. *Biochemistry* 1981;20(18):5132–40. [PubMed: 6945871]
10. Burgess BK, Werland S, Newton WE, Stiefel EI. Nitrogenase reactivity: insight into the nitrogen-fixing process through hydrogen-inhibition and HD-forming reactions. *Biochemistry* 1981;20(18): 5140–6. [PubMed: 6945872]
11. Fisher K, Dilworth MJ, Newton WE. Differential effects on N<sub>2</sub> binding and reduction, HD formation, and azide reduction with  $\alpha$ -195His- and  $\alpha$ -191Gln-substituted MoFe proteins of *Azotobacter vinelandii* nitrogenase. *Biochemistry* 2000;39(50):15570–15577. [PubMed: 11112544]
12. Yandulov DV, Schrock RR. Catalytic Reduction of Dinitrogen to Ammonia at a Single Molybdenum Center. *Science* (Washington, DC, United States) 2003;301(5629):76–78.
13. Chatt J, Dilworth JR, Richards RL. Recent advances in the chemistry of nitrogen fixation. *Chem. Rev* 1978;78:589–625.
14. Hettterscheid DGH, Hanna BS, Schrock RR. Molybdenum Triamidoamine Systems. Reactions Involving Dihydrogen Relevant to Catalytic Reduction of Dinitrogen. *Inorganic Chemistry* (Washington, DC, United States) 2009;48(17):8569–8577.
15. Lukoyanov D, Pelmeshnikov V, Maeser N, Laryukhin M, Yang TC, Noodleman L, Dean D, Case D, Seefeldt L, Hoffman B. Testing if the Interstitial Atom, X, of the Nitrogenase Molybdenum-Iron Cofactor is N or C: ENDOR, ESEEM, and DFT Studies of the S = 3/2 Resting State in Multiple Environments. *Inorganic Chemistry* 2007;46(26):11437–11449. [PubMed: 18027933]
16. Igarashi RY, Laryukhin M, Santos PCD, Lee H-I, Dean DR, Seefeldt LC, Hoffman BM. Trapping H- Bound to the Nitrogenase FeMo-cofactor Active Site During H<sub>2</sub> Evolution: Characterization by ENDOR Spectroscopy. *Journal of the American Chemical Society* 2005;127(17):6231–6241. [PubMed: 15853328]
17. Yandulov DV, Schrock RR, Rheingold AL, Ceccarelli C, Davis WM. Synthesis and Reactions of Molybdenum Triamidoamine Complexes Containing Hexaisopropylterphenyl Substituents. *Inorganic Chemistry* 2003;42(3):796–813. [PubMed: 12562193]
18. Davydov R, Makris TM, Kofman V, Werst DW, Sligar SG, Hoffman BM. Hydroxylation of Camphor by Reduced oxy-Cytochrome P450cam: Mechanistic Implications of EPR and ENDOR of Catalytic Intermediates in Native and Mutant Enzymes. *Journal of the American Chemical Society* 2001;123:1403–1415. [PubMed: 11456714]
19. Pilbrow, JR. Transition Ion Electron Paramagnetic Resonance. Clarendon Press; Oxford: 1990.
20. Werst MM, Davoust CE, Hoffman BM. Ligand Spin Densities in Blue Copper Proteins by Q-band <sup>1</sup>H and <sup>14</sup>N ENDOR Spectroscopy. *Journal of the American Chemical Society* 1991;113(5):1533–1538.
21. Davoust CE, Doan PE, Hoffman BM. Q-Band Pulsed Electron Spin-Echo Spectrometer and Its Application to ENDOR and ESEEM. *Journal of Magnetic Resonance* 1996;119:38–44.
22. Zipse H, Artin E, Wnuk S, Lohman GJS, Martino D, Griffin RG, Kacprzak S, Kaupp M, Hoffman B, Bennati M, Stubbe J, Lees N. Structure of the nucleotide radical formed during reaction of CDP/TTP with the E441Q- $\alpha$ 2 $\beta$ 2 of E. coli ribonucleotide reductase. *Journal of the American Chemical Society* 2009;131:200–211. [PubMed: 19128178]
23. Hoffman BM, DeRose VJ, Ong JL, Davoust CE. Sensitivity Enhancement in Field-Modulated CW ENDOR via RF Bandwidth Broadening. *Journal of Magnetic Resonance* 1994;110:52–57.
24. Schweiger, A.; Jeschke, G. Principles of Pulse Electron Paramagnetic Resonance. Oxford University Press; Oxford, UK: 2001. p. 578
25. Epel B, Gromov I, Stoll S, Schweiger A, Goldfarb D. Spectrometer manager: A versatile control software for pulse EPR spectrometers. *Concepts in Magnetic Resonance Part B: Magnetic Resonance Engineering* 2005;26B(1):36–45.
26. Hoffman BM. Electron nuclear double resonance (ENDOR) of metalloenzymes. *Accounts of Chemical Research* 1991;24:164–170.



27. Doan, PE. The Past, Present, and Future of Orientation-Selected ENDOR Analysis: Solving the Challenges of Dipolar-Coupled Nuclei.. In: Telser, J., editor. *Paramagnetic Resonance of Metallobiomolecules*. American Chemical Society; 2003. p. 55-81.
28. Doan PE. *Journal of Magnetic Resonance*. 2009 manuscript in preparation.
29. Epel B, Poppl A, Manikandan P, Vega S, Goldfarb D. The Effect of Spin Relaxation on ENDOR Spectra Recorded at High Magnetic Fields and Low Temperatures. *J. Magn. Reson* 2001;148(2): 388–397. [PubMed: 11237646]
30. Yang T-C, Hoffman BM. A Davies/Hahn Multi-Sequence for Studies of Spin Relaxation in Pulsed ENDOR. *Journal of Magnetic Resonance* 2006;181:280–286. [PubMed: 16777447]
31. McNaughton RL, Chin JM, Weare WW, Schrock RR, Hoffman BM. EPR Study of the Low-Spin [ $d^3$ ;  $S = 1/2$ ], Jahn-Teller-Active, Dinitrogen Complex of a Molybdenum Trisamidoamine. *Journal of the American Chemical Society* 2007;129(12):3480–3481. [PubMed: 17341079]
32. Benton PMC, Laryukhin M, Mayer SM, Hoffman BM, Dean DR, Seefeldt LC. Localization of a Substrate Binding Site on FeMo-Cofactor in Nitrogenase: Trapping Propargyl Alcohol with an  $\alpha$ -70-Substituted MoFe Protein. *Biochemistry* 2003;42(30):9102–9109. [PubMed: 12885243]
33. Weber S, Kay CWM, Bacher A, Richter G, Bittl R. Probing the N(5)-H Bond of the Isoalloxazine Moiety of Flavin Radicals by X- and W-Band Pulsed Electron-Nuclear Double Resonance. *ChemPhysChem* 2005;6(2):292–299. [PubMed: 15751352]
34. The shoulders observed on the ENDOR spectra at  $g_3$  and  $g_1$  can be straightforwardly accounted for in the simulations by increasing the EPR linewidth. While the simulation does not perfectly reproduce the effect in the data, the differences are acceptable given the approximations used for calculating the EPR linewidth in the simulation program. Further information and a figure are provided in the Supplemental Information.
35. Snetsinger PA, Chasteen ND, van Willigen H. Structural Analysis of a Low-Spin Cyanide Adduct of Iron(III) Transferrin by Angle-Selected  $\{+13\}C$  ENDOR Spectroscopy. *Journal of the American Chemical Society* 1990;112(22):8155–8160.
36. Kubas GJ, Burns CJ, Eckert J, Johnson SW, Larson AC, Vergamini PJ, Unkefer CJ, Khalsa GRK, Jackson SA, Eisenstein O. Neutron structure and inelastic-neutron-scattering and theoretical studies of molybdenum complex  $Mo(CO)(H_2)[(C_6D_5)_2PC_2H_4P(C_6D_5)_2]2.4.5C_6D_6$ , a complex with an extremely low barrier to hydrogen rotation. Implications on the reaction coordinate for H-H cleavage to dihydride. *Journal of the American Chemical Society* 1993;115(2):569–81.
37. Shin JH, Churchill DG, Bridgewater BM, Pang K, Parkin G. Hydride, halide, methyl, carbonyl, and chalcogenido derivatives of permethylmolybdenocene. *Inorganica Chimica Acta* 2006;359(9):2942–2955.
38. Martins LMDRS, Alegria ECBA, Hughes DL, Frausto da Silva JJR, Pombeiro AJL. Syntheses and properties of hydride-cyanamide and derived hydrogen-cyanamide complexes of molybdenum(IV). Crystal structure of  $[MoH_2(NCNH_2)_2(Ph_2PCH_2CH_2PPh_2)_2][BF_4]_2$ . *Dalton Transactions* 2003; (19):3743–3750.
39. Ritleng V, Yandulov DV, Weare WW, Schrock RR, Hock AS, Davis WM. Molybdenum Triamidoamine Complexes that Contain Hexa-tert-butylterphenyl, Hexamethylterphenyl, or p-Bromohexaisopropylterphenyl Substituents. An Examination of Some Catalyst Variations for the Catalytic Reduction of Dinitrogen. *Journal of the American Chemical Society* 2004;126(19):6150–6163. [PubMed: 15137780]
40. Lucken, EAC. *Nuclear Quadrupole Coupling Constants*. Academic Press; New York: 1969. p. 360
41. Density Functional Theory (DFT) calculations were performed with the Amsterdam Density Functional (ADF) software package (ADF version 2007.01, SCM, Theoretical Chemistry, Vrije Universiteit, Amsterdam, The Netherlands, <http://www.scm.com>) with a BLYP functional in the spin-unrestricted formalism. Geometry optimization calculations on  $[MoH]^+$  and  $MoHNH$  used a TZ2P basis set with a small core potential for all atoms. For calculation of all hyperfine, quadrupole and g-tensor values, no core potential was used. All calculations used a reduced structure for Mo in which the HIPT groups were replaced with phenyls.
42. Abragam, A.; Bleaney, B. *Electron Paramagnetic Resonance of Transition Ions*. Dover Publications, Inc.; New York: 1986.
43. Bersuker, IB. *The Jahn-Teller Effect*. First ed.. Cambridge University Press; 2006. p. 54-62.



44. Force constants (K) for Mo-H and Mo-N were calculated using IR stretching frequencies of  $1748\text{ cm}^{-1}$  and  $453\text{ cm}^{-1}$ , respectively, yielding  $K(\text{Mo-H}) = 160\text{ N m}^{-1}$  (Yandulov, et. al) and  $K(\text{Mo-N}) = 148\text{ N m}^{-1}$  (Stephan, et. al).
45. Stephan GC, Peters G, Lehnert N, Habeck CM, Naether C, Tuczek F. Bonding, activation, and protonation of dinitrogen on a molybdenum pentaphosphine complex - comparison to trans-bis (dinitrogen) and -nitrile-dinitrogen complexes with tetraphosphine coordination. *Canadian Journal of Chemistry* 2005;83(4):385–402.
46. Bersuker, IB. *The Jahn-Teller Effect*. First ed.. Cambridge University Press; Cambridge: 2006. p. 353-478.

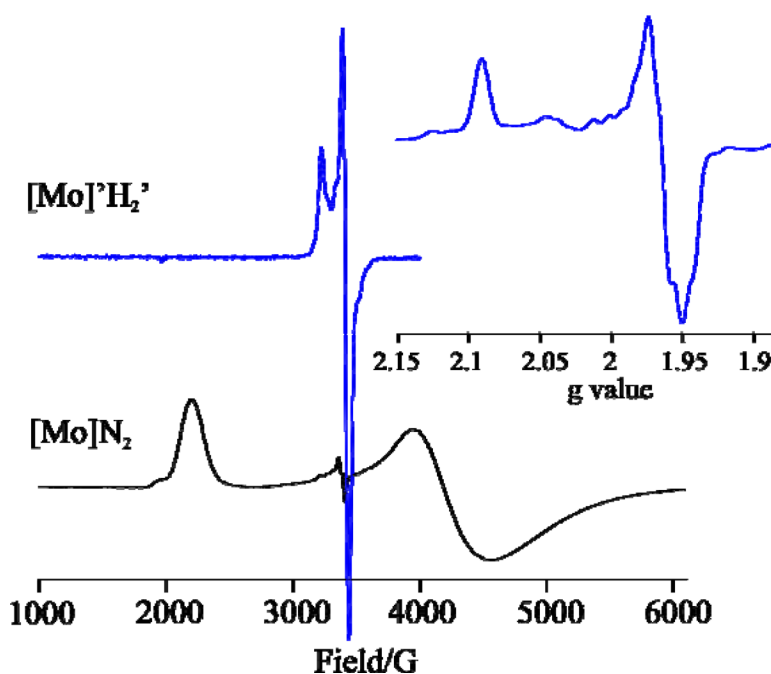


**Figure 1.**

Comparison between 4K X-band CW EPR of  $\text{MoN}_2$  (black),  $g_{\parallel} = 3.03$ ,  $g_{\perp} = 1.6$ , and **1** (blue),  $g = [2.086, 1.961, 1.947]$ , both in frozen toluene solution. *Inset:* Expanded view of the spectra of **1** in frozen toluene solution. *Conditions:* microwave frequency, 9.365 GHz; modulation amplitude, 2.8 G; microwave power, 0.632 mW; temperature, 11 K; scan time, 120 s; time constant, 80 ms.

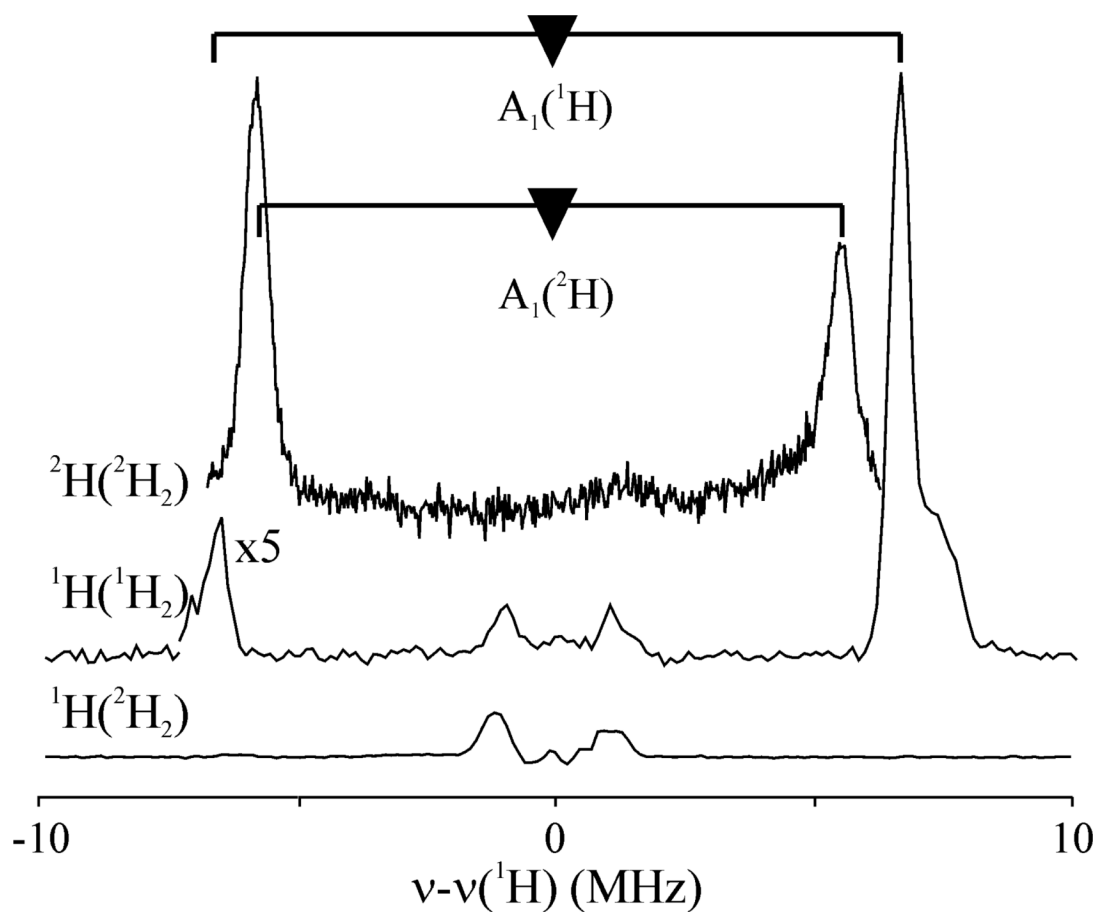


**Figure 2.**  $^1\text{H}$  stochastic CW ENDOR and  $^2\text{H}$  Mims ENDOR spectra of **1** and **1(D)** at  $g_1$ . The frequency axis of the  $^1\text{H}$  spectrum has been scaled by the ratio of the nuclear  $g$  values ( $g_n(^1\text{H})/g_n(^2\text{H}) = 6.51$ ), thus allowing it to be plotted on the  $^1\text{H}$  frequency axis.  
*Conditions:*  $^1\text{H}$  stochastic CW: microwave frequency, 35.273–35.305 GHz; modulation amplitude, 0.66 G; microwave power, 0.1 mW; temperature 2 K; and the RF excitation was broadened to 50 kHz.  $^2\text{H}$  Mims: microwave frequency, 34.914–34.967 GHz;  $\pi/2 = 50$  ns;  $\tau = 500$  ns; repetition time, 20 ms; RF pulse length, 30  $\mu\text{s}$ ; 1 shot per RF point; and the RF was randomly hopped.

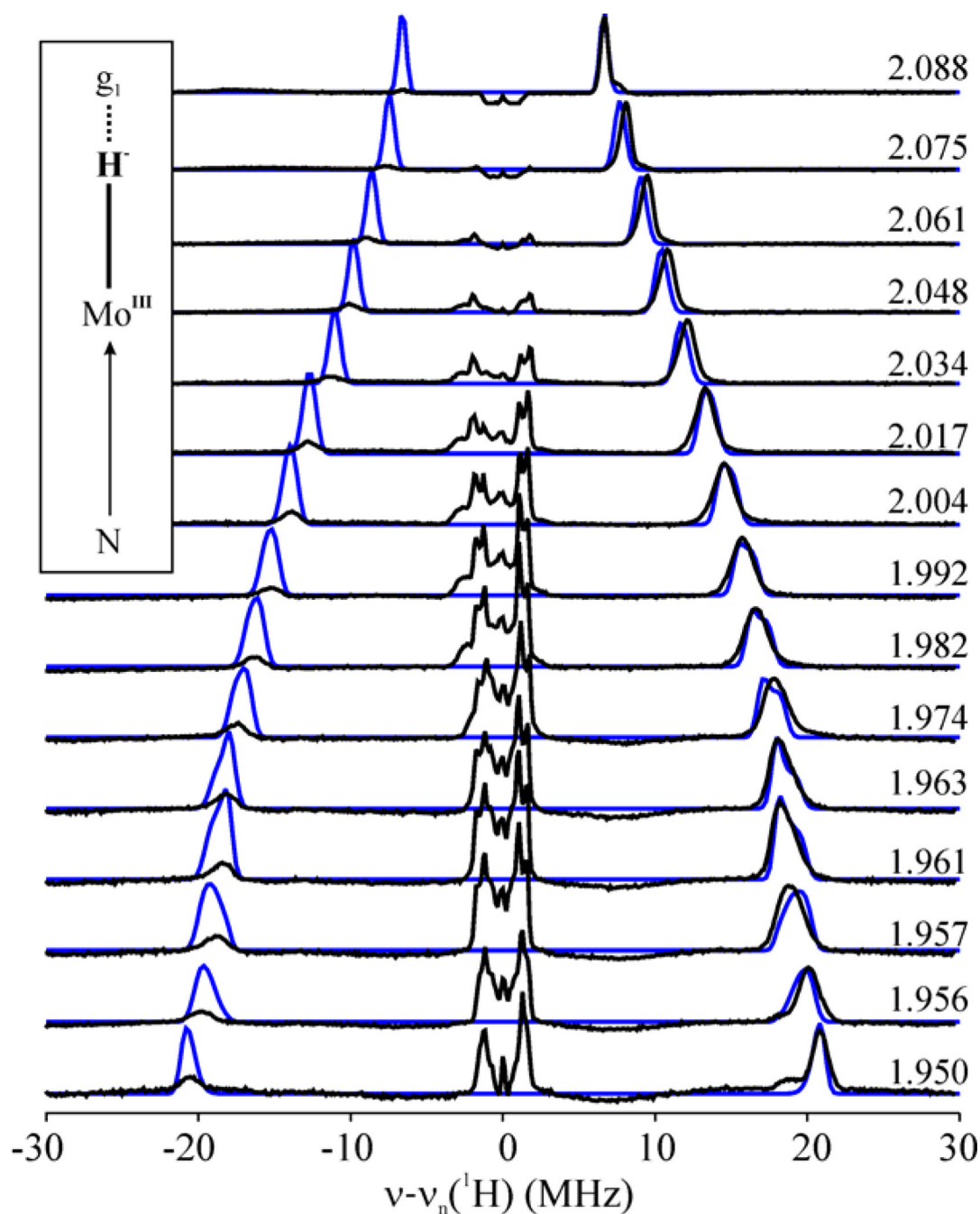


**Figure 3.**

Q-band stochastic-field modulation-detected 2D field-frequency ENDOR pattern for **1** (black) with simulations of the hydride (blue). *Conditions:* microwave frequency, 35.305 GHz; modulation amplitude, 0.66 G; temperature, 2 K; stochastic sequence (delay/sample/RF), 0.75/1.25/0.5 ms; rf excitation was broadened to 50 kHz. *Simulation parameters:*  $g = [2.086, 1.961, 1.947]$ ;  $A = [13\ 36\ 42.5]$  MHz, coaxial with  $g$ ; EPR linewidth, 100 MHz; and ENDOR linewidth, 0.5 MHz. The EPR/ENDOR linewidths were deliberately set somewhat smaller than those which best reproduce the measurements to emphasize the absence of splittings in the peaks that occur when  $g$  and  $A$  are non-coaxial (see Figure 4 and Supplementary Material);

this procedure gives rise to the hints of structure near  $g \sim 1.97$  and the absence of a shoulder for the simulations at  $g_3 = 1.95$  and  $g_1 = 2.088$ .

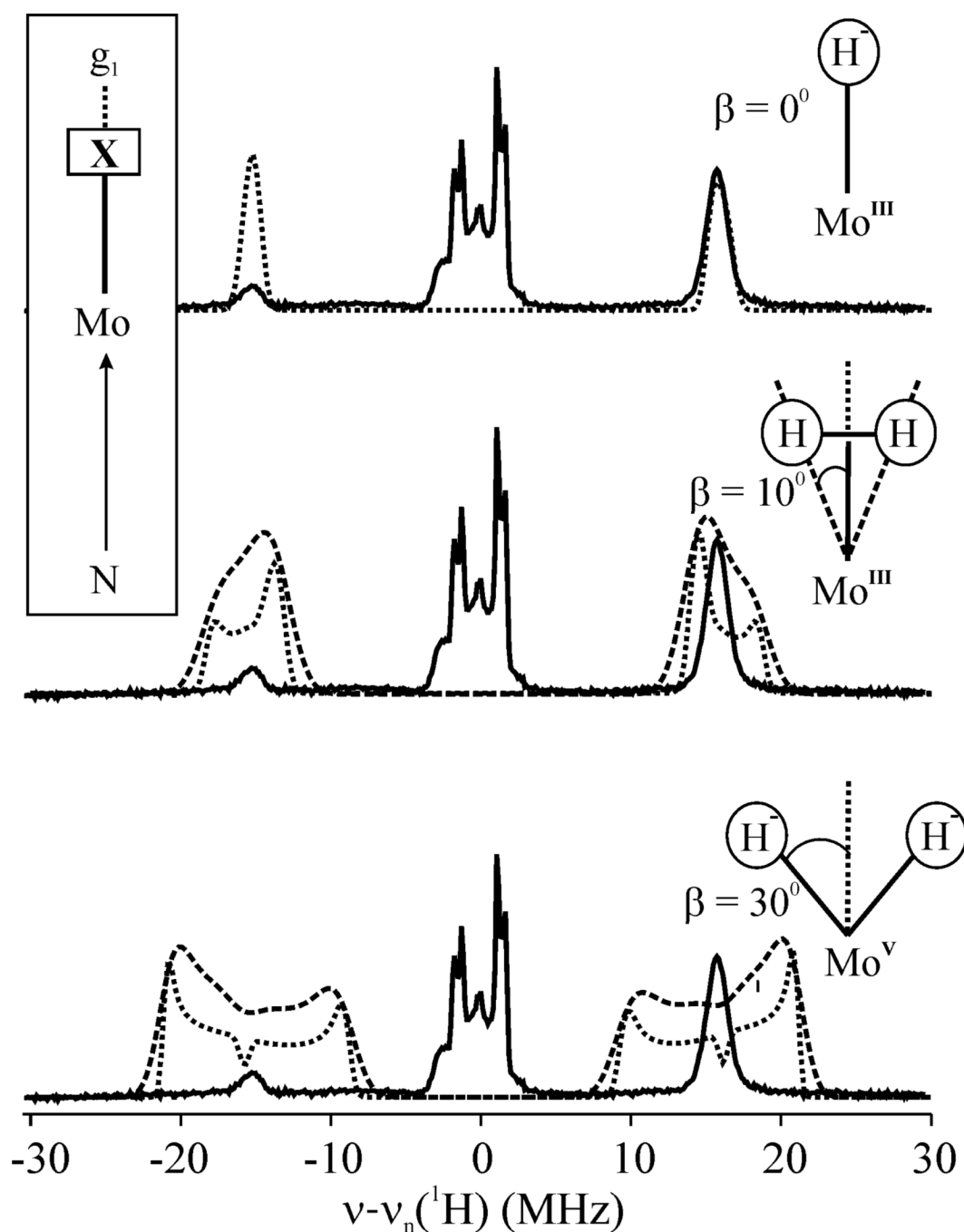


**Figure 4.**

Simulations of  $^1\text{H}$  ENDOR spectra for models of the reaction product of  $\text{MoN}_2$  with  $\text{H}_2$ , for the spectrum at  $g = 1.99$ . Simulations are based on the hyperfine tensor determined through the fit to the 2D field frequency plot of Figure 3 ( $\mathbf{A} = [13 \ 36.5 \ 42]$  MHz), but with the dipolar interaction rotated by the angle ( $\beta$ ) between the hydrogen nuclei and the  $g_1$  axis, taken to lie along the  $\text{Mo-N}_{\text{ax}}$  bond. *Top*:  $\text{Mo-H}^-$  bond along  $g_1$ ,  $\beta = 0^\circ$ ; *Middle*: Dihydrogen complex; each hydrogen hyperfine tensor is rotated relative to  $\mathbf{g}$  by  $\beta = 10^\circ$ ; *Bottom*: Dihydride,  $\beta = 30^\circ$ . Simulation parameters:  $\mathbf{g} = [2.086, 1.961, 1.947]$ ,  $\beta$  as indicated. In the second and third cases, two simulations are given, one with small EPR and ENDOR linewidths (150 and 0.5



MHz; dotted lines) to show resolved features, the other with larger EPR and ENDOR linewidths (300 MHz and 2 MHz; dashed lines) to show that these features could not be masked.

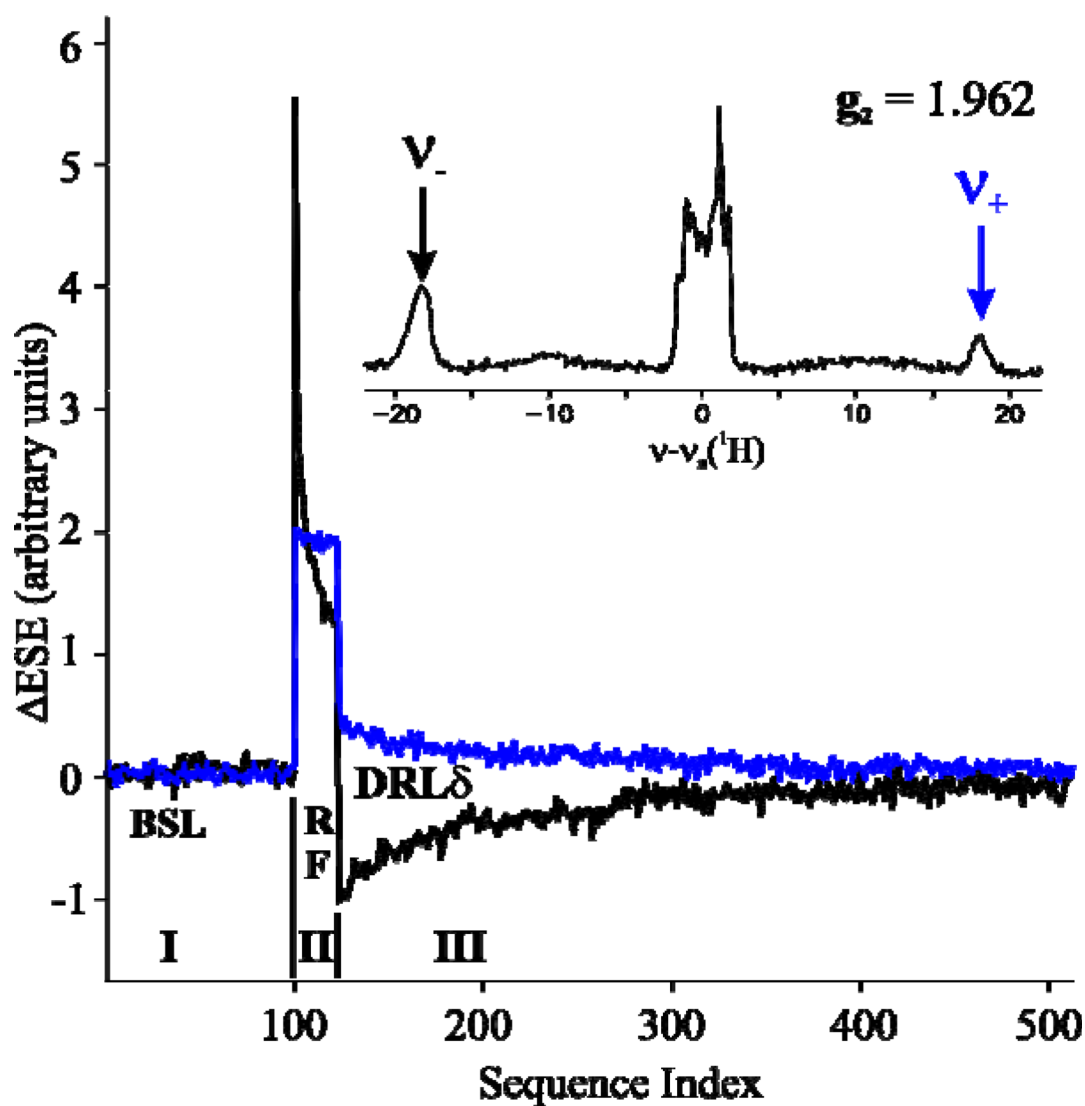


**Figure 5.**

PESTRE spectra measured at the  $\nu_+$  (blue) and  $\nu_-$  (black) peaks of the hydride ENDOR response in **1** at  $g_2 = 1.961$ . *Inset.* Davies  $^1\text{H}$  ENDOR spectrum at  $g_2$ . The frequencies at which a PESTRE spectrum was measured are notated by arrows. *Conditions.* PESTRE: microwave frequency, 34.998 GHz;  $\pi = 200$  ns;  $\tau = 600$  ns; repetition rate, 40 ms;  $t_{\text{rf}} = 30$   $\mu\text{s}$ ; RF frequency, 72.4 MHz ( $\nu_+$ ) and 36.0 MHz ( $\nu_-$ );  $^1\text{H}$  ENDOR:  $\pi = 200$  ns;  $\tau = 600$  ns; repetition rate, 40 ms;  $t_{\text{rf}} = 30$   $\mu\text{s}$ ; RF frequency randomly hopped.

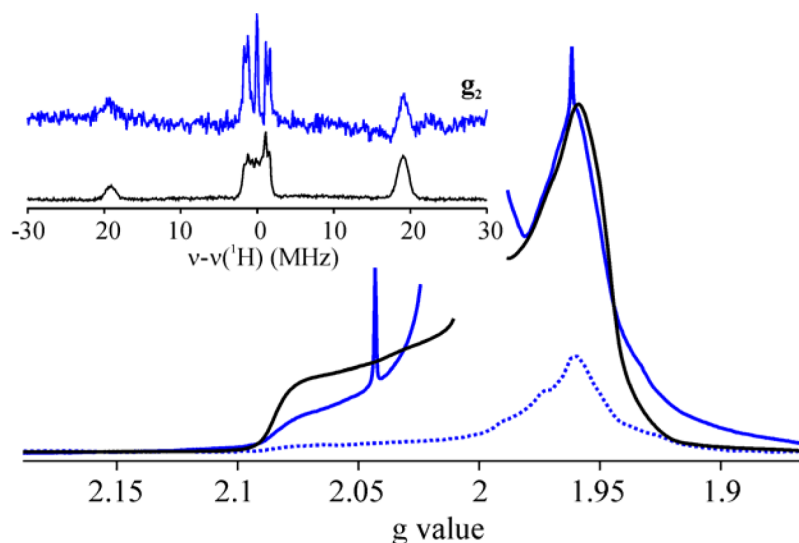


**Figure 6.**

35 GHz CW EPR of **1** (black), **2** before cryoreduction, (dashed blue), and **2** after cryoreduction (blue). The cryoreduced **2** shows a four-fold increase in the reduced species relative to that found in the non-reduced **2**.  $\gamma$ -irradiation also generates organic radicals whose signal is truncated for clarity, as well as hydrogen atoms within the quartz tubes, which contribute the characteristic sharp hyperfine doublet with  $|A(^1\text{H})| = 507$  G. *Inset*: 35 GHz  $^1\text{H}$  stochastic field-modulated ENDOR spectra of cryoreduced **2** (blue) and **1** (black) measured at  $g_3 = 1.947$ .

*Conditions*: EPR of **2**: microwave frequency, 35.289 GHz; microwave power, 0.1 mW; modulation amplitude, 0.33 G; time constant, 64 ms; scan time, 2 minutes; receiver gain divided out of the spectra of **2**; intensity of **1** arbitrarily adjusted to match intensity at  $g_2$  of **2**. ENDOR: microwave frequency, 35.231 GHz; modulation amplitude, 0.3 G; temperature, 2 K; stochastic sequence (delay/sample/RF), 0.75/1.25/0.5 ms; rf excitation was broadened to 50 kHz.

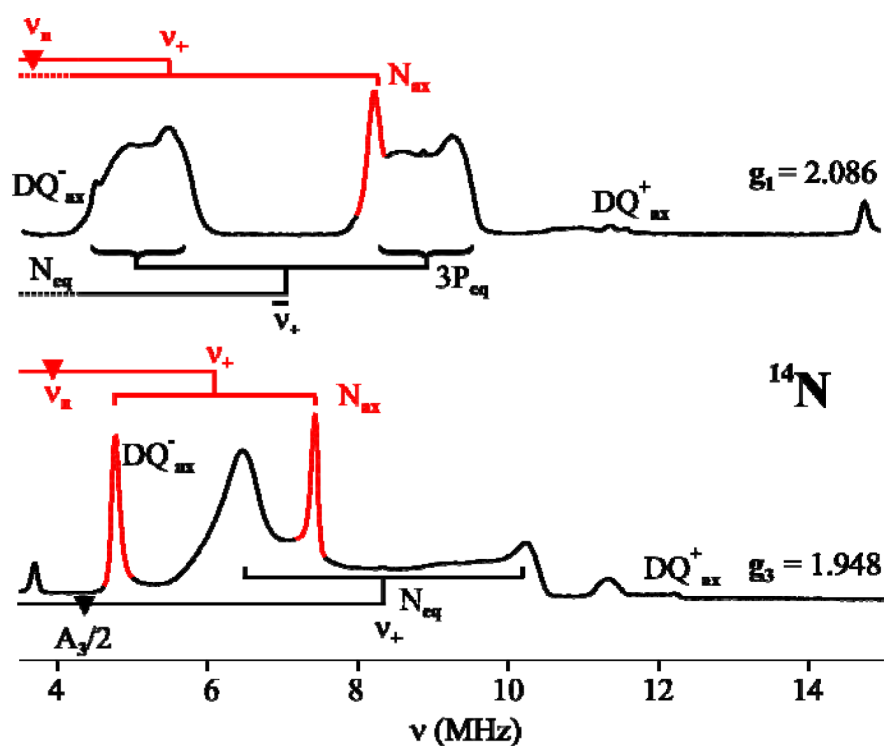


**Figure 7.** Davies  $^{14}\text{N}$  pulse ENDOR of **1** at  $g_1 = 2.086$  and  $g_3 = 1.947$ . The axial nitrogen ( $\text{N}_{\text{ax}}$ ) and equatorial nitrogen ( $\text{N}_{\text{eq}}$ ) quadrupole split peaks for the  $\nu_+$  manifold are labeled. The ‘double quantum’ ( $\Delta m_I = \pm 2$ ) transitions for both the alpha and beta electron manifolds are labeled. *Conditions:* microwave frequency, 34.998 GHz;  $\pi = 200$  ns;  $\tau = 1000$  ns;  $t_{\text{rf}} = 30$   $\mu\text{s}$ ; repetition rate, 20 ms; RF frequency randomly hopped.

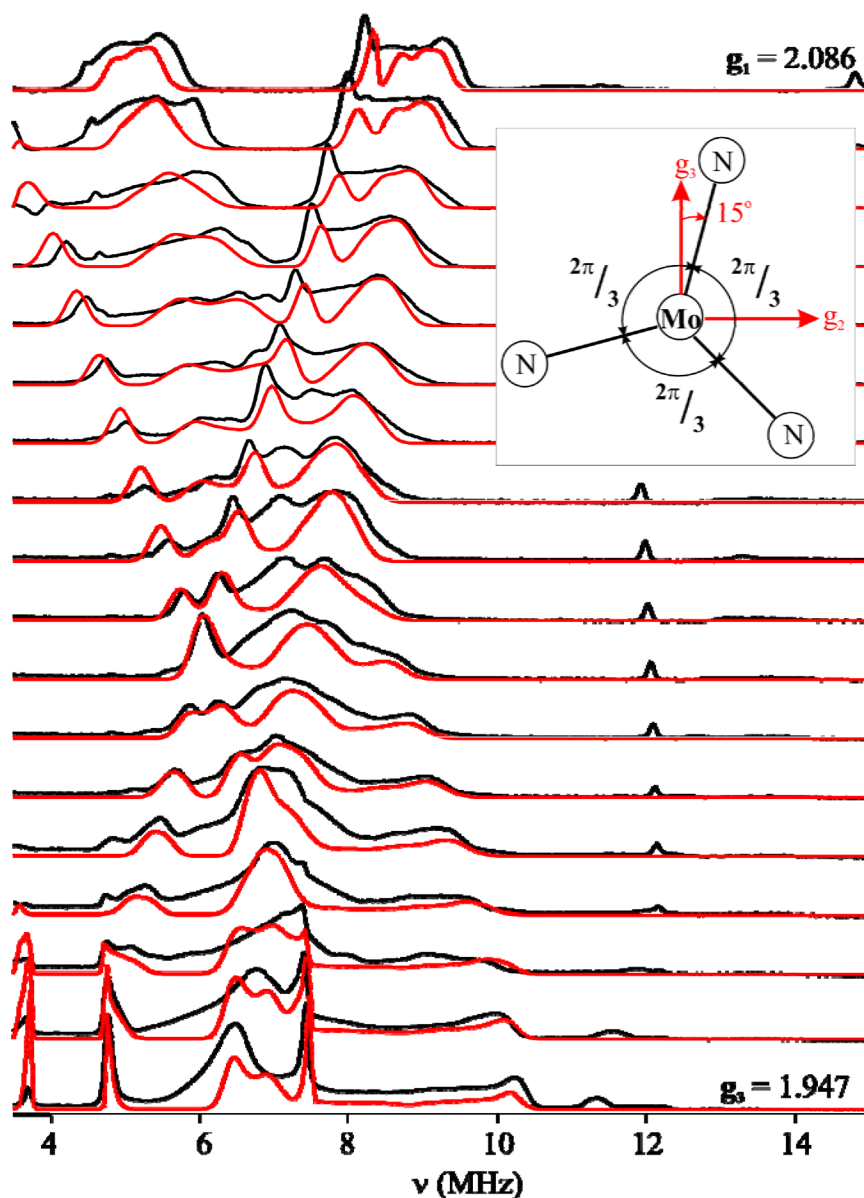


**Figure 8.**

Davies  $^{14}\text{N}$  pulse ENDOR of **1**, 2D field-frequency pattern with simulations. The simulation pattern is the sum of the simulations for the axial nitrogen and three sets of three simulations for the equatorial nitrogens. *Inset.* The rotation angle  $\alpha$  is defined as a rotation around the  $g_1$  axis (normal to the plane of the equatorial nitrogens). The angles utilized for the three equatorial nitrogens are indicated in the diagram. *Simulation parameters:* microwave frequency, 34.998 GHz;  $\mathbf{g} = [2.086, 1.961, 1.947]$ ; EPR linewidth, 150 MHz;  $g_1 = z$ ; *Axial N:*  $\mathbf{A} = [3.95, 4, 4.05]$  MHz;  $\mathbf{P} = [-1.82, 0.91, 0.91]$  MHz; ENDOR linewidth, 0.01 MHz;  $\mathbf{g}$ ,  $\mathbf{A}$ , and  $\mathbf{P}$  are coaxial; allowed transitions included; *Equatorial N:*  $\mathbf{A} = [\{5.39, 6.25, 7.11\}, 5.8, 8.7]$  MHz;  $\mathbf{P} = [-1.33, 0.03, 1.3]$  MHz;  $(\alpha \beta \gamma) = (\{15, 135, 75\}, 0, 0)$ , ENDOR linewidth, 0.25 MHz, only plus manifold include.

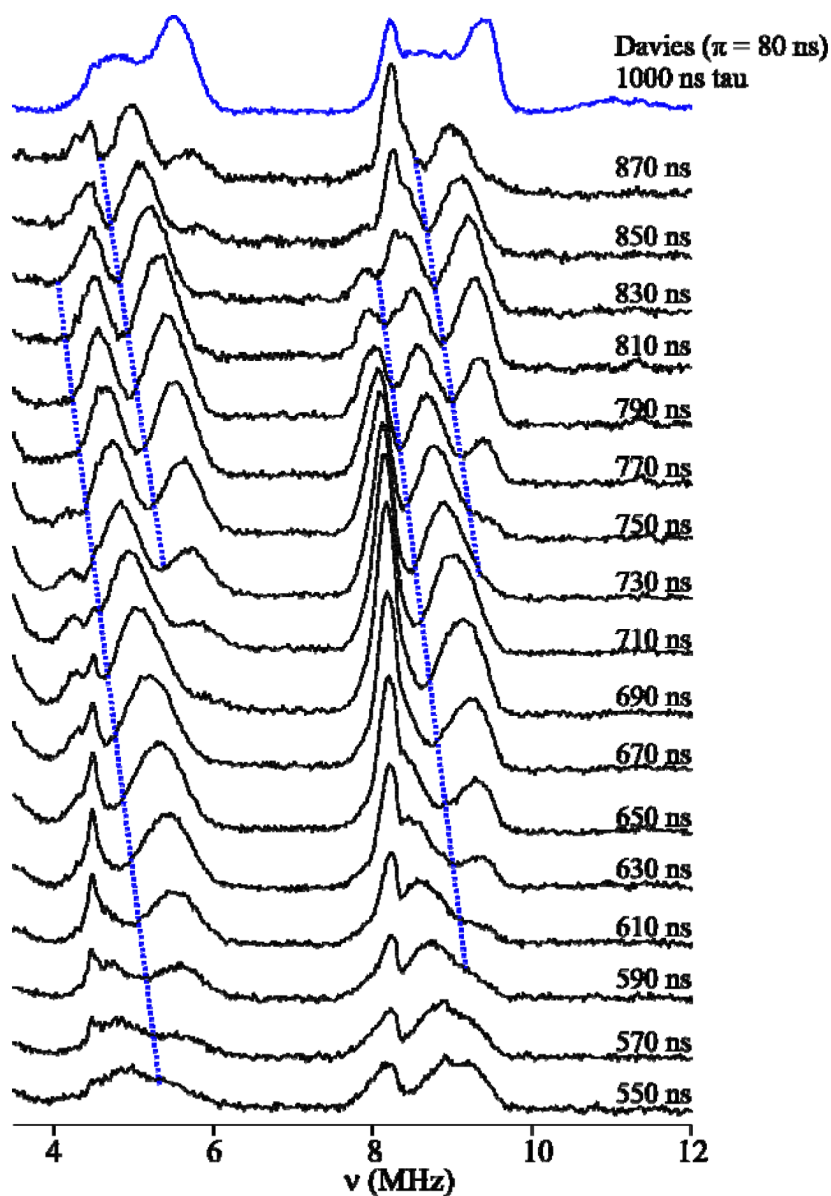


**Figure 9.**

Mims  $^{14}\text{N}$  pulse ENDOR of **1** at  $g_1 = 2.086$ . The value of  $\tau$  is varied from 550 to 870 ns to observe the effect of hyperfine suppression on the  $^{14}\text{N}$   $\nu_+$  ENDOR pattern. Due to the quadrupole splitting inherent to the  $^{14}\text{N}$  pattern, observation of suppression occurs for a given hyperfine coupling at the frequencies  $A \pm \frac{3}{2}P$  MHz. This splitting is delineated by the separation between the dashed blue lines. *Conditions:* microwave frequency, 35.017 GHz; repetition time, 20 ms;  $\pi/2 = 50$  ms;  $\tau = 550$ -870 ns;  $t_{\text{rf}} = 30$   $\mu\text{s}$ ; RF frequency randomly hopped.



